inter.noise
HAMBURG 2016

Aeroacoustic analysis of a NACA 0015 airfoil with Gurney flap based on time-resolved PIV measurements

Xueqing ZHANG[1], Andrea SCIACCHITANO and Stefan PRÖBSTING
Department of Aerodynamics, Delft University of Technology
Kluyverweg 2, 2629HT Delft,The Netherlands

ABSTRACT
The present study investigates the feasibility of high-lift devices noise prediction based on measurements of time-resolved particle image velocimetry (TR-PIV). The model under investigation is a NACA 0015 airfoil with Gurney flap with height of 6% chord length. The velocity fields around and downstream the Gurney flap are measured by PIV and are used for the PIV-based noise predictions. The predictions are assessed via microphone measurements. Since the Gurney flap height is much smaller than the emitted acoustic wavelength, the source of noise can be considered compact and the integral implementation of Curle's analogy based on the unsteady aerodynamic loads can be followed. The results are compared with the simultaneous microphone measurements in terms of time histories and power spectra. The integral formulation of Curle's analogy yields acoustic sound pressure levels in good agreement with the simultaneous microphone measurements for the tonal component. All the calculated far-field noise power spectra reproduce the peak at vortex shedding frequency, which also agrees well with the microphone measurements.

Keywords: Time-resolved PIV, Gurney flap noise, Curle's aeroacoustic analogy

1. INTRODUCTION

With the implementation of the large bypass ratio turbo-fan engines on civil aircraft that remarkably reduce the level of engine noise, the attention of noise control has shifted to the reduction of airframe noise. The deployment of high-lift devices during takeoff and landing is one of the major source of this airframe noise [1]. Traditional approaches of acoustic assessment rely mainly on microphone (array) measurements (for instance Hutcheson and Brooks [2]) or instantaneous flow fields obtained from numerical CFD codes, such URANS, LES (for instance Casalino et al. [3]). However, the former fails in providing the mechanism of noise generation, while the latter becomes prohibitive in the operating Reynolds number range of real aircraft.

The seminal paper in aeroacoustics published in 1952 by M. J. Lighthill [4] established a mathematical relation between the unsteady flow field quantities and the radiated sound. With the rapid advancement in hardware and software in the past decade, PIV has become a powerful tool in capturing the instantaneous velocity field with a comparatively high combined spatial and temporal dynamic range when compared to other measurement methods. In recent years, the application of time-resolved PIV (TR-PIV) in aeroacoustic investigations became particularly of interest. Henning et al. have performed a series of synchronized TR-PIV and microphone measurements on a cylinder wake [5], rod-airfoil configuration [6], cold jet [7] and high-lift device [8] to identify the flow patterns responsible for the noise emission. Noise predictions based on TR-PIV data have also been carried out successfully. Pröbsting et al. [9, 10] have employed time-resolved PIV in combination with non-stationary signal processing for the analysis of the source field around an airfoil generating tonal noise. Haigermoser [11] derived the acoustic emission of a cavity flow based on planar TR-PIV measurements in a water tunnel. Koschatzky et al. [12] applied Curle's analogy and vortex sound

[1]email: x634zhan@uwaterloo.ca

theory to the noise prediction of an open, two-dimensional shallow cavity. Lorenzoni et al. [13] investigated the acoustic emission from vortex-structure of a rod-airfoil configuration. More recently, Pröbsting et al. [14] demonstrated the prediction of broadband noise, caused by the interaction of the turbulent boundary layer with the trailing edge, based on time-resolved tomographic PIV.

The spatial gradients of the hydrodynamic pressure can be derived from the momentum equation (Equation 1), where σ is the contributions of the viscosity.

$$\rho\frac{D\mathbf{v}}{Dt} = \frac{\partial(\rho\mathbf{v})}{\partial t} + \rho\mathbf{v}\cdot\bigtriangledown\mathbf{v} = -\nabla p + \nabla\cdot\sigma \tag{1}$$

For 2D PIV measurement, the pressure field can be reconstructed either by direct spatial integration [15] or by solution of a Poisson equation on a cross-sectional plane in the flow (Equation 2) with appropriate boundary conditions derived from the momentum equations [16], where the notation ∇_{xy} indicates taking the in-plane divergence of the pressure gradient.

$$\nabla_{xy}\cdot\nabla p = \frac{\partial^2 p}{\partial x^2} + \frac{\partial^2 p}{\partial y^2} = \rho f_{xy}(\mathbf{v}) \tag{2}$$

The former method introduces an accumulation of random errors along the integration path. The omni-directional virtual boundary integration scheme developed by Liu and Katz [17] enables integration with minimized effect of local random error. The latter approach yields different performance depending on the choice of Lagrangian or Eulerian formulation of the pressure gradients. Violato et al. [18] compared the two approaches on a rod-airfoil configuration and offered guidelines for the choice of experimental parameters according to the approach adopted. De Kat and van Oudheusden [19] further assessed the experimental viability of the approaches in the reconstruction of instantaneous pressure field, giving emphasis on the flow features of convecting vortices. Under the assumption of incompressible flow, the aerodynamic loads can further be derived on the basis of pressure reconstruction with the momentum balanced equation proposed by Kurtulus et al. [20]. Alternatively, Noca et al. [21] derived and compared three methods for the evaluation of time-dependent forces circumventing the step of pressure reconstruction.

The present study aims at proving the feasibility of quantitative acoustic prediction of lift-enhancing devices based on TR-PIV measurements, where the Gurney flap serves as a simplified model of the flap used in civil aviation. Curle's analogy can be applied based on either the reconstructed surface pressure or the evaluated aerodynamic loads. The present study focuses on the latter approach, the predictions given by which are compared with the simultaneous far-field acoustic pressure recorded by the microphone. The outcome is a first step towards optical diagnostics of the aeroacoustic emissions due to the flow field around a high-lift device.

2. AEROACOUSTIC MODEL

Curle's analogy is a solution to Lighthill's equation with the presence of stationary, rigid and solid surfaces in the flow. Under the circumstances where the flow is of high Reynolds and low Mach number, the contribution of viscous and quadrupole terms is negligible [22, 23], and the analogy can be reduced to:

$$p'(\mathbf{x},t) = -\frac{x_j}{4\pi c_0|\mathbf{x}|}\frac{\partial}{\partial t}\int_{\delta V_y}\left.\frac{p'\delta_{ij}}{r}\right|_{t=t_e} n_i dS \tag{3}$$

where $p' = p - p_0$ indicates the pressure deviation from the equilibrium value p_0. On the left hand side, p' represents the pressure fluctuation in the far-field, namely, the propagating acoustic pressure in a quiescent medium. In contrast, p' in the integral on the right hand side indicates the local pressure fluctuation on the surface of the solid body. The subscript $t = t_e$ in the integral indicates that that the noise produced at time $t_e = t - r/c_0$ in the source region reaches the listener's location in the far field at time t.

When the submerged solid body satisfies the compact body assumption $L/\lambda << Ma << 1$, indicating that the acoustic wave propagates much faster than the convection of the vortices, an uniform retarded time

$t_e = t - R/c_0$ can be assumed for the sources distributed on the solid surface. Thus, the integral of pressure can be substituted by the instantaneous aerodynamic loads [24]:

$$p'(\mathbf{x}, t) = -\frac{R_j}{4\pi c_0 R^2} \frac{\partial F_j(t_e)}{\partial t} \tag{4}$$

Equation 4 is known as the Gutin's principle for compact and rigid body [24], where R_j is the j^{th} component of the position vector originating from the airfoil leading edge pointing to the listener and F_j is the aerodynamic force. Equation 3 and 4 are referred to respectively as the 'distributed' and the 'lumped' formulations in the following sections.

3. EXPERIMENTS

3.1 Experimental setup

Simultaneous planar PIV and microphone measurements were carried out in the vertical low turbulence wind tunnel (V-tunnel) at Delft University of Technology. A circular-to-square transition flow duct was installed to accommodate a closed test section with exit dimensions of $40 \times 40cm^2$. A NACA 0015 model of 20 cm chord, wetted span of 40 cm and with a Gurney flap of 12 mm height (6% of the chord) was placed vertically in the wind tunnel with its geometric angle of attack set to 4°. The detachable trailing edge of the model was made out of plexiglass to allow the passage of laser light, such that the velocity field on both pressure and suction side of the trailing edge could be captured simultaneously. The boundary layer was tripped at the quarter chord location with roughness elements of 0.84 mm nominal grain size. The configuration was examined for a nominal free stream velocity of 20 m/s with incoming turbulent level below 0.1%.

Two-component TR-PIV was used to obtain the planar velocity field around and downstream the Gurney flap. The light sheet was placed at the mid-span section of the airfoil. For the reason of spatial resolution, two Photron Fastcam SA1.1 cameras with CMOS sensors, placed facing each other on both sides of the test section, were used for image acquisition.To achieve a higher acquisition frequency of 5 kHz, the sensors of the two cameras were cropped to $704 \times 704px^2$. Each camera was equipped with a Nikon Micro-Nikkor 105 mm lens to capture a field of view (FOV) of $80 \times 80mm^2$, resulting in a combined field of view of roughly $80 \times 140mm^2$ (Figure 1) and a magnification factor $M = 0.176$, with numerical aperture set to $f_\# = 2.8$ to collect sufficient light. Under the setting of such a numerical aperture, the particle image diameter is around $0.2\ px$ at the plane of measurement. To avoid peak-locking, the focal plane of the cameras was slightly shifted with respect to measurement plane to obtain a particle image diameter larger than $1\ px$.

The illumination was provided by a Quantronix Nd-YLF laser (2×12 mJ/pulse at 2.7 kHz) and the flow was seeded with water-glycol based fog with droplets of mean diameter of $1\ \mu m$.

The recording comprises 5773 image pairs acquired at the frequency of $5\ kHz$ and with a separation of $50\ \mu s$ between the frames of one image pair, corresponding to a displacement of $1\ mm$ (approximately 9 pixels) in the free stream. The illumination and imaging system are synchronized with a LaVision High-Speed controller and the acquisition is controlled by the DAVIS 8 software. The latter is also used for the image processing and interrogation.

The images are processed with sequential cross-correlation algorithm with multi-pass iterations of decreasing interrogation window sizes from 64×64, 50% overlap, 2-pass, square-shaped window to 32×32 to 75% overlap, 3-pass, round-shaped window. Vector post-processing is applied to remove the outliers. The spurious velocity vectors are detected by means of the normalized median test, developed by Westerweel and Scarano in 2005 [25].

The simultaneous acoustic measurements were performed by a set of four LinearX-M53 microphones, placed at a fixed distance of $1.3\ m$ from the airfoil trailing edge. The microphones are placed at angles, with respect to the horizontal line, of 30°, 18°, 0° and -18° respectively, as shown in Figure 2.

Table 1 gives an overview of the experimental parameters of the synchronized planar PIV and microphone measurements.

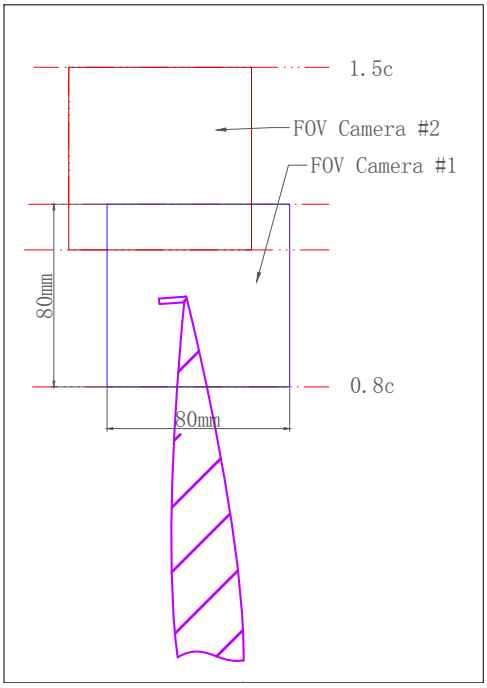

Figure 1. Field of View for two-camera recording

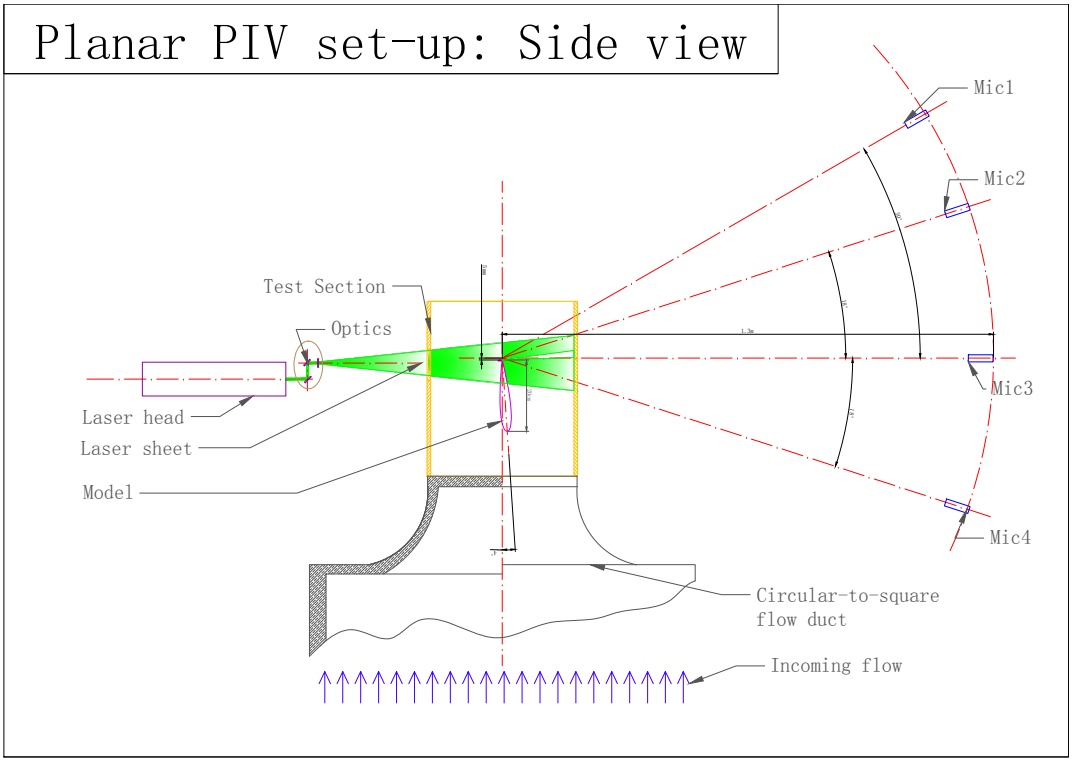

Figure 2. Schematic of set-up for synchronized planar PIV and microphone measurements

Table 1. Parameters for synchronized planar PIV and microphone measurements

Parameter	Value	Unit
Field of View (FOV), for each camera	80×80	mm^2
Field of View (FOV), combined	80×140	mm^2
Sensor size	704×704	pxs
Magnification factor, M	0.176	–
Focal length, f	105 (both cameras)	mm
Numerical aperture, $f_{\#}$	2.8 (both cameras)	–
PIV acquisition frequency, f_s	5	kHz
Pulse separation, dt	50	μs
Number of images, N	5773	–
Microphone placement (distance from the trailing edge)	1.3	m
Microphone acquisition frequency, f_{mic}	51.2	kHz

3.2 Planar PIV measurements

A snapshot of the instantaneous visualization of the transverse (u-component) and streamwise (v-component) velocity fields around and downstream the Gurney flap is provided by Figure 3. In the wake region downstream the Gurney flap, a deficit in the streamwise velocity component can be observed, and the alternation of positive and negative transverse velocity indicates the existence of large vortical structures. Correspondingly, the counter-rotating vortices can be observed from the time sequence of instantaneous vorticity fields in Figure 4, illustrated by the coherent regions marked in red (counter-clockwise) and blue (clockwise). The vortices shed at the trailing edge are convected downstream at an average spacing of 5 cm with a velocity of around 16.7 m/s, which is approximately 83% of the free stream velocity. The spectral analysis of the fluctuating velocity depicts a peak frequency at 314.9 Hz, corresponding to a period of $T_{shed} = 0.32ms$. The peak frequency coincides with the peak frequency measured by the far-field microphones, as can be observed in Figure 8 (bottom, red curve), indicating that the coherent vortex shedding is responsible for the tonal component of the radiated noise. The sequence of instantaneous snapshots of vorticity fields are presented in Figure 4. The vorticity downstream the Gurney flap exhibits a coherence pattern as well as a distinguishable convection process.

4. RESULTS AND DISCUSSIONS

4.1 Integral loads evaluation

Kurtulus et al. [20] estimated the unsteady forces on a square cylinder from the velocity field measured by planar TRPIV. The general integral form of the momentum balance is written as:

$$\vec{F}(t) = -\rho \iiint_{\mathcal{V}} \frac{\partial \vec{V}}{\partial t} d\mathcal{V} - \rho \iint_S (\vec{V} \cdot \vec{n}) \vec{V} dS - \iint_S p\vec{n} dS + \iint_S \bar{\bar{\tau}} \vec{n} dS \tag{5}$$

In this case the planar PIV measurement cannot resolve the out-of-plane velocity, and therefore only the velocity components along the measurement plane xy are considered. In addition, with the outer boundary of the control volume sufficiently far from the body surface, the viscous effect (the contributions of $\bar{\bar{\tau}}$) is neglected, resulting in Equation 6, where u,v are velocity components defined in the x and y coordinate

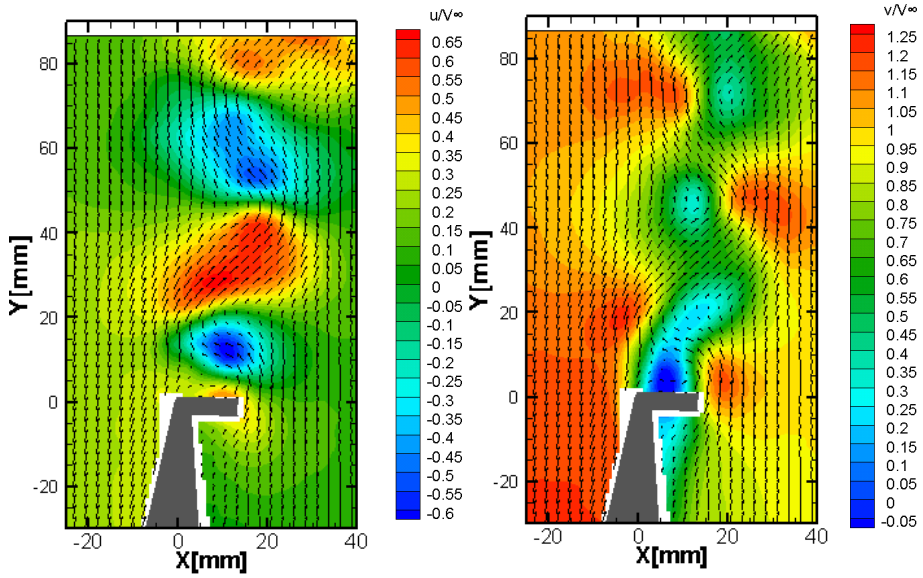

Figure 3: A snapshot of the non-dimensionalized instantaneous transverse velocity (left) and streamwise velocity (right)

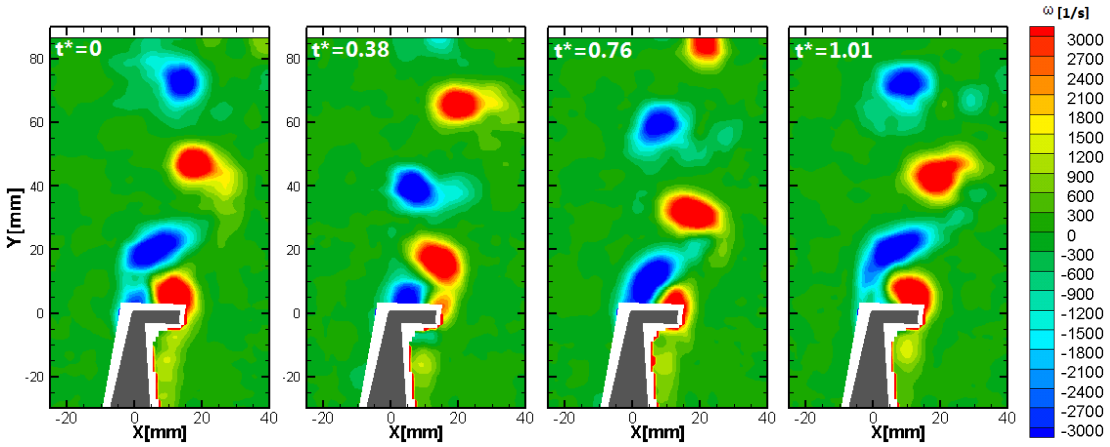

Figure 4: Time sequence of the instantaneous vorticity fields at normalized time instant $t^* = t/T_{shed}$ during approximately one shedding cycle

direction.

$$\begin{bmatrix} D \\ L \end{bmatrix} = -\rho \iint_V \begin{bmatrix} \frac{\partial u}{\partial t} dxdy \\ \frac{\partial v}{\partial t} dxdy \end{bmatrix} + \rho \oint_S \begin{bmatrix} -u^2 dy + uvdx \\ -uvdy + v^2 dx \end{bmatrix} + \oint_S \begin{bmatrix} -pdy \\ pdx \end{bmatrix} \tag{6}$$

Kurtulus et al. [20] also proposed a robust procedure for the evaluation of the pressure terms on the control surface in Equation 6. The pressure is related to the velocity by the Navier-Stokes equations (Equation 1) and the spatial gradients of pressure can be expressed in either the Eulerian (Equation 7) or the Lagrangian formulation (Equation 8) as:

$$\nabla p = -\rho \left(\frac{\partial \mathbf{v}}{\partial t} + (\mathbf{v} \cdot \nabla)\mathbf{v} - \nu \nabla^2 \mathbf{v} \right) \tag{7}$$

$$\nabla p = -\rho \left(\frac{D\mathbf{v}}{Dt} - \nu \nabla^2 \mathbf{v} \right) \tag{8}$$

As shown in Figure 2 of reference [20], the part of control surface encountered by the wake is defined as 'viscous region', where pressure is obtained by integrating Equation 8, but neglecting the viscous contribution. To minimize the effect of error propagation in the process of spatial integration, outside the wake, pressure is estimated by Bernoulli equation. In such a way, pressure in the wake region can be resolved by integrating from both edges of the wake, and the end point of integration, located in the inviscid region, can be compared with the value given by Bernoulli equation. The discrepancy between the integration result and the Bernoulli equation (Equation 9) can then be used to redistribute the discrepancy along the viscous region with a linear weighting function. The above mentioned technique is derived and applied to the incompressible scenario. The threshold for viscous region is set as $\varepsilon > 1.5 \times 10^4 s^{-2}$ as in pressure reconstruction, where ε is the local value of enstrophy, defined as the square of local vorticity:

$$p = P_\infty + \frac{1}{2}\rho V_\infty^2 - \frac{1}{2}\rho(u^2 + v^2) \tag{9}$$

$$\varepsilon = |\overrightarrow{\omega}|^2 \tag{10}$$

Time series of lift and drag are plotted in Figure 5 and 6, with the aerodynamic loads plotted in black and the first, second and third term in Equation 6 plotted respectively in green, blue and red. The plots also show the mean value of the aerodynamic loads, plotted in magenta.

Periodicity can be observed in the reconstructed aerodynamic loads and the components. For lift, the fluctuations are primarily attributed to the volume integral of the time derivatives of the velocity and the surface integral of the convection terms, while for the drag, the major components are the two surface integral terms. However, it would be imprudent to neglect any of the three components in both lift and drag, when looking closely at the order of magnitude and considering their contribution to the phase of the overall fluctuation.

The resulting power spectra of the aerodynamic loads evaluated from the PIV measurement on FOV 2 are presented in Figure 7. Both the lift and the drag peak at the frequency of $314.9Hz$, which is consistent with the shedding frequency as expected.

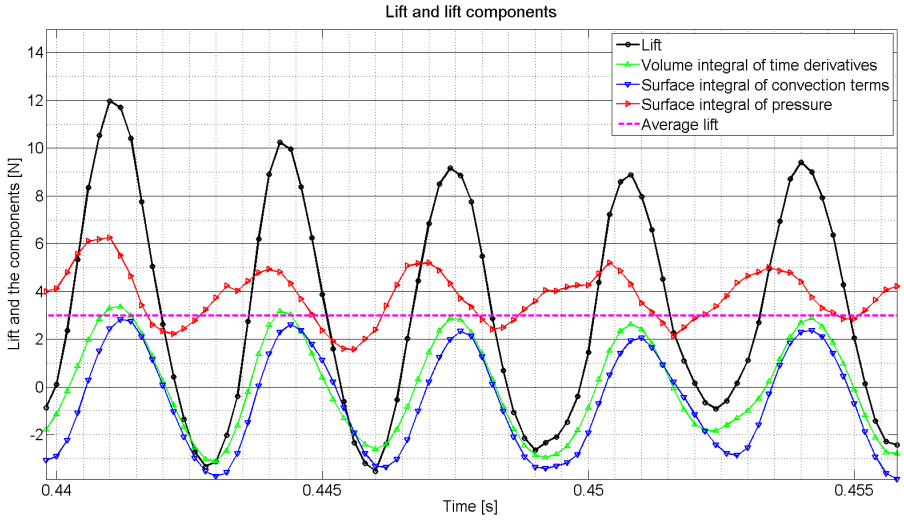

Figure 5. Time series of lift and lift components evaluated from PIV measurements.

4.2 Acoustic prediction

As shown in Equation 4, the pressure fluctuation at the location of the listener (or microphone) is the sum of the contribution received at time instant t by the listener and emitted at (different) retarded time instant(s)

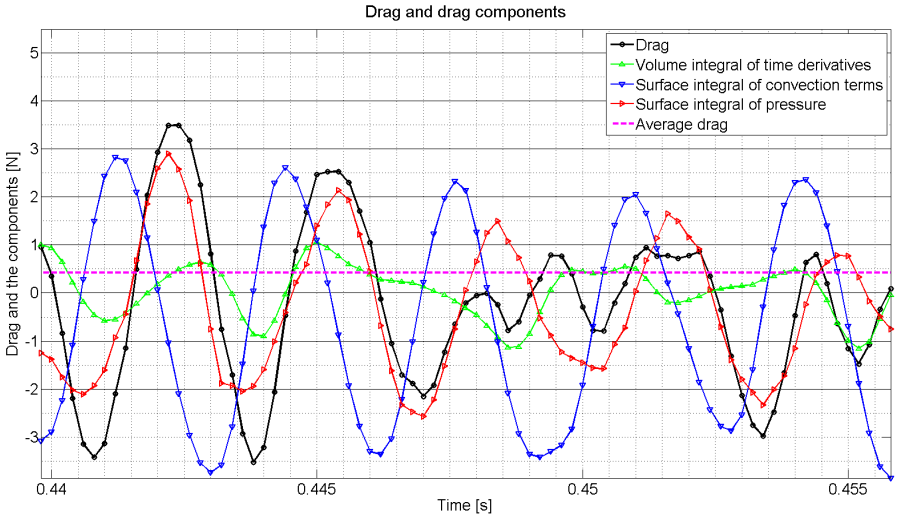

Figure 6. Time series of drag and drag components evaluated from PIV measurements.

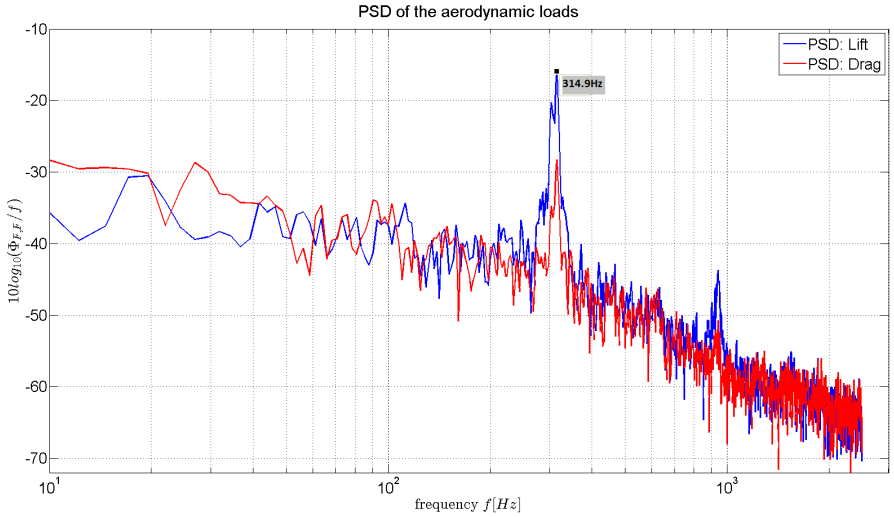

Figure 7. Power spectra ($\Delta f = 2.4Hz$) of lift and drag evaluated from PIV measurements.

t_e over the source region, namely the fluctuation in aerodynamic forces at t_e. The values of $t - t_e$ of this case are evaluated for the solid surface locations within the PIV field of view and are summarized in Table 2.

It can be observed that the largest difference in retarded time is $0.1ms$ along the surface of airfoil. Under

Table 2. Value of $t - t_e$ for microphones with respect to the sources distributed on the airfoil surface

Listener	min.$(t - t_e)[ms]$	max.$(t - t_e)[ms]$	mean.$(t - t_e)[ms]$	max.$(\Delta(t - t_e))[ms]$
Microphone 1	4.3	4.4	4.4	0.1
Microphone 2	4.0	4.0	4.0	0
Microphone 3	3.8	3.9	3.8	0.1
Microphone 4	3.9	4.0	4.0	0.1

the sampling rate of the current study ($5kHz$), the time interval between two snapshots of velocity field is $0.2ms$. With further observation of the mean value of $(t - t_e)$, it can be inferred that source locations with a value of $(t - t_e)$ different from the mean value only account a small portion of airfoil surface. The observa-

tion of retarded time inversely testifies that the experimental set-up for the current study satisfies the compact source assumption, and thus each microphone can be assigned with the respective mean value of $(t - t_e)$ for the calculation of retarded time.

Based on the aerodynamic loads evaluated from the PIV measurement, Equation 4 is implemented to reconstruct the far-field acoustic pressure. The distance from the airfoil trailing edge and each respective microphone is used to calculate the uniform retarded time. The values of $t - t_e$ of the microphones coincides with the average values listed in Table 2.

Time series of the far-field acoustic pressure in time series, both the microphone measurements and the reconstruction from PIV measurements based on the full spanwise coherence assumption are shown in Figure 8 (top). The two measurements roughly share the same period and phase. However, the maximum coefficients obtained from the cross-correlation of the far-field pressure measured by microphone and that evaluated by PIV are 0.19.

As expected, the amplitude predicted by PIV measurements is larger than that measured by the microphones at all four locations of microphones, since in reality the flow is intrinsically 3D and the spanwise coherence length is shorter than the span.

Figure 8 (bottom) shows the power spectra of the far-field acoustic pressure. The blue curve and the red curve show respectively the predictions of PIV and the measurements of microphones, and both peak at a frequency of around $315Hz$, which is consistent with the peak frequency of aerodynamic loads. The latter consistency is expected, since at the Mach number of the current study ($Ma_\infty = 0.059$), the Doppler effect is negligible, the frequency reaching the receiver should be equal to the frequency emitted by the source.

The extra green curve in Figure 8 (bottom) offers a comparison of the power spectra of the clean NACA 0015 (microphone recordings performed at same locations), which consists of only broadband components. The absence of frequency peak on the power spectra of a NACA 0015 without Gurney flap provides an additional indication that the tonal noise generated by the model with Gurney flap should be attributed to the presence of the Gurney flap.

Compared to the tonal component, for the broadband components, less agreement between the PIV prediction and the microphone measurements is retrieved. The microphone spectra feature a rise in amplitude in frequency range below 100 Hz. The low frequency components in the microphone spectra have been shown to be caused by the wind tunnel operation noise, concluded from the preliminary background measurements and the measurements on the airfoil model without Gurney flap (Figure 8 (bottom), green curve). Self-evidently, the background noise of wind tunnel operation cannot be revealed by acoustic computation based on velocity measurements.

The sharp decay in magnitude observed at $1000Hz$ in Figure 8 has no physical meaning. The artificial magnitude reduction is mainly due to the numerical smoothing of the signal in the calculation of the time derivatives. Comparison of the effect of the discrete method used for time derivatives was presented by Lorenzoni (2008)[26], suggesting that the central scheme (which is applied in the present study) is more effective in magnitude reduction since a wider kernel is used for the computation of the differences.

The amplitude of computed acoustic spectra does not decay in the high frequency range as in the spectra of microphone measurements since the high frequency components are more susceptible to experimental and numerical noise which can be attributed to:

- The effect of 3D motion with high intensity directly downstream the Gurney flap.
- Measurement noise.
- Aliasing due to finite sampling frequency.

5. CONCLUSION

In the present study, the feasibility of acoustic evaluation of the high-lift devices based on the time-resolved PIV velocity measurements was investigated. The investigation was performed on the configuration

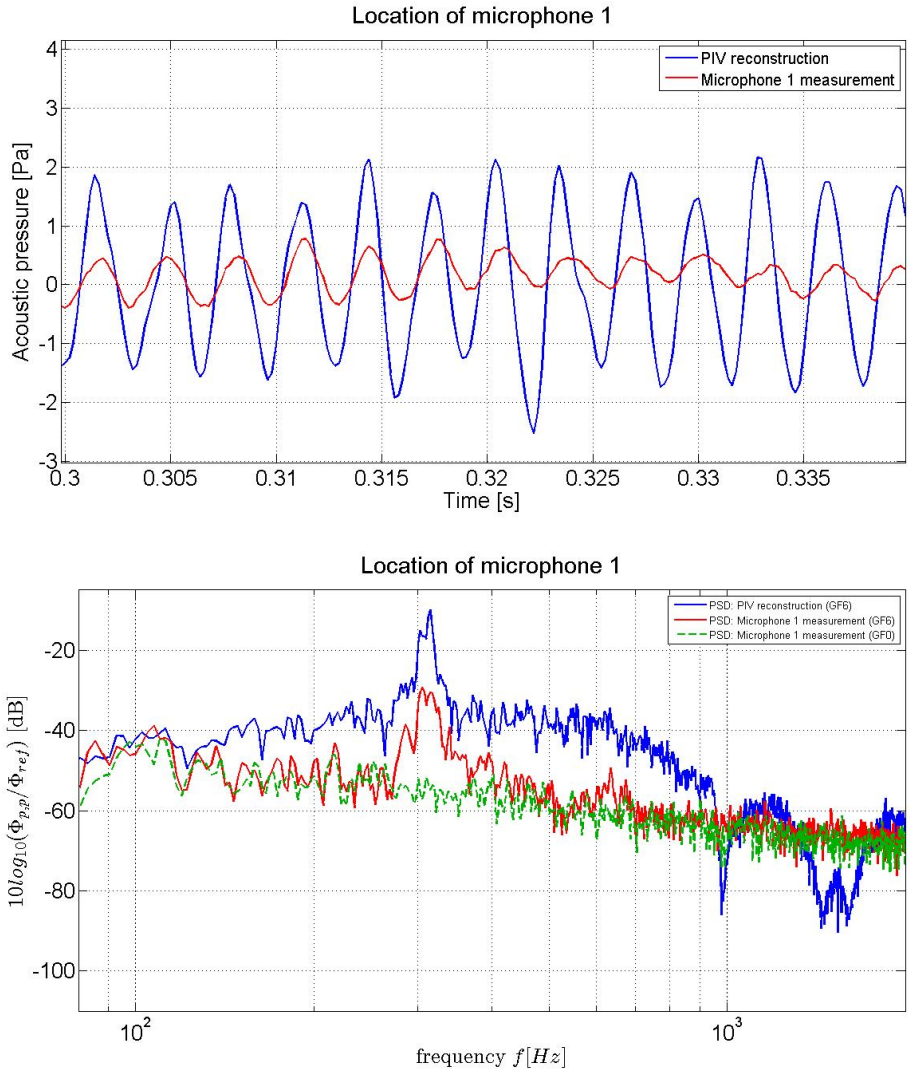

Figure 8: Time series (top) and power spectra (bottom: $\Delta f = 2.4Hz$, $\Phi_{ref} = 1Pa^2/Hz$) of far-field acoustic pressure evaluated by lumped formulation of Curle's analogy based on full span coherence assumption from PIV measurements in comparison with the simultaneous microphone measurement at the location of Microphone 1.

of NACA 0015 airfoil with a Gurney flap of the height of 6% the chord length. The velocity fields were measured by TR-PIV around and downstream the Gurney flap. Coherence pattern and distinguishable convection downstream the Gurney flap can be observed in the instantaneous vorticity fields derived from the velocity measurements.

The velocity measurements were used to reconstruct the instantaneous aerodynamic loads by means of the momentum balance. The evaluated fluctuations in aerodynamic loads constituted the source terms in the 'lumped' formulation of Curle's analogy. The predictions of sound pressure level by means of Curle's analogy were compared with the far-field microphone measurements at corresponding locations obtained simultaneously with the PIV measurement. The frequency of the tonal noise is consistent with the frequency of vortex shedding. The power spectra of the fluctuations of velocity, aerodynamic loads and far-field pressure did not indicate the existence of a second shedding mode for this configuration as the one proposed by Troolin et al. [27].

The computed noise spectra revealed fair agreement with the microphone measurements for the tonal component and the narrow frequency band around the peak. The sound pressure level predicted under the assumption of perfect correlation over the entire span yielded over-estimation in sound pressure level as ex-

pected at all four microphone locations.

The present investigation proved TR-PIV an effective approach in the prediction of radiated noise of the trailing edge with Gurney flap provided that the requirements of spatio-temporal resolution can be met by the experimental apparatus. It remains to be explored the effectiveness of narrowing the over-estimation in the predicted sound pressure level with respect to the microphone measured ones with the approach of equivalent coherence length proposed by Kato et al. [28] and proven to work reasonably well by literatures such as [13], [29] and [30]. Further improvements can be made with the utilization of tomographic PIV that offers the 3D-time resolved velocity information for the acoustic analogies and source identification. As a next step, it would be instructive to extend the investigation to high-lift devices with more complicated structures with noise spectra of broadband nature.

REFERENCES

[1] Roger M. Aeroacoustics: Some theoretical background – The acoustic analogy Noise from moving surfaces. In: Course, Computational aeroacoustics; Rhode Saint Genese, Belgium; 2006. .

[2] Hutcheson F, Brooks T. Effects of angle of attack and velocity on trailing edge noise determined using microphone array measurements. International Journal of Aeroacoustics. 2006;5(1):p. 39–66.

[3] Casalino D, Jacob M, Roger M. Prediction of rod-airfoil interaction noise using the Ffowcs-Williams-Hawkings analogy. AIAA journal. 2003;41(2):p. 182–191.

[4] Lighthill MJ. On sound generated aerodynamically I General theory. In: Proceedings of the Royal Society of London A: Mathematical, Physical and Engineering Sciences. vol. 211. The Royal Society; 1952. p. p. 564–587.

[5] Henning A, Kaepernick K, Ehrenfried K, Koop L, Dillmann A. Investigation of aeroacoustic noise generation by simultaneous particle image velocimetry and microphone measurements. Experiments in fluids. 2008;45(6):p. 1073–1085.

[6] Henning A, Koop L, Ehrenfried K. Simultaneous particle image velocimetry and microphone array measurements on a rod-airfoil configuration. AIAA journal. 2010;48(10):p. 2263–2273.

[7] Henning A, Schröder A, Koop L, Agocs J. Causality correlation analysis on a cold jet by means of simultaneous particle image velocimetry and microphone measurements. Journal of Sound and Vibration. 2013;332(13):p. 3148–3162.

[8] Henning A, Wrede B, Geisler R. Aeroacoustic investigation of a high-lift device by means of synchronized PIV and microphone measurements. In: 16th Int Symp on Applications of Laser Techniques to Fluid Mechanics, Lisbon, Portugal; 2012. p. p. 1–11.

[9] Pröbsting S, Serpieri J, Scarano F. Experimental investigation of aerofoil tonal noise generation. J Fluid Mech. 2014;vol. 747:p. 656–687.

[10] Pröbsting S, Scarano F, Morris SC. Regimes of tonal noise on an airfoil at moderate Reynolds number. J Fluid Mech. 2015;vol. 780:p. 407–438.

[11] Haigermoser C. Application of an acoustic analogy to PIV data from rectangular cavity flows. Experiments in fluids. 2009;47(1):p. 145–157.

[12] Koschatzky V, Westerweel J, Boersma BJ. Comparison of two acoustic analogies applied to experimental PIV data for cavity sound emission estimation. In: Proceedings of the 16th AIAA/CEAS Aeroacoustic Conference; 2010. p. p. 7–9.

[13] Lorenzoni V, Tuinstra M, Scarano F. On the use of time-resolved particle image velocimetry for the investigation of rod–airfoil aeroacoustics. Journal of Sound and Vibration. 2012;331(23):p. 5012–5027.

[14] Pröbsting S, Tuinstra M, Scarano F. Trailing edge noise estimation by tomographic Particle Image Velocimetry. J Sound Vib. 2015;vol. 346:p. 117–138.

[15] Baur T, Köngeter J. PIV with high temporal resolution for the determination of local pressure reductions from coherent turbulence phenomena. In: 3rd international workshop on particle image velocimetry, Santa Barbara, CA, USA; 1999. .

[16] Gurka R, Liberzon A, Hefetz D, Rubinstein D, Shavit U. Computation of pressure distribution using PIV velocity data. In: Workshop on particle image velocimetry. vol. 2; 1999. .

[17] Liu X, Katz J. Instantaneous pressure and material acceleration measurements using a four-exposure PIV system. Experiments in Fluids. 2006;41(2):p. 227–240.

[18] Violato D, Moore P, Scarano F. Lagrangian and Eulerian pressure field evaluation of rod-airfoil flow from time-resolved tomographic PIV. Experiments in fluids. 2011;50(4):p. 1057–1070.

[19] De Kat R, Van Oudheusden B. Instantaneous planar pressure determination from PIV in turbulent flow. Experiments in fluids. 2012;52(5):p. 1089–1106.

[20] Kurtulus D, Scarano F, David L. Unsteady aerodynamic forces estimation on a square cylinder by TR-PIV. Experiments in Fluids. 2007;42(2):p. 185–196.

[21] Noca F, Shiels D, Jeon D. A comparison of methods for evaluating time-dependent fluid dynamic forces on bodies, using only velocity fields and their derivatives. Journal of Fluids and Structures. 1999;13(5):p. 551–578.

[22] Goldstein ME. Aeroacoustics. New York, McGraw-Hill International Book Co, 1976 305 p. 1976;1.

[23] Wang M, Freund JB, Lele SK. Computational prediction of flow-generated sound. Annu Rev Fluid Mech. 2006;38:p. 483–512.

[24] Powell A. Theory of vortex sound. The journal of the acoustical society of America. 1964;vol. 36:p. 177–195.

[25] Westerweel J, Scarano F. Universal outlier detection for PIV data. Experiments in Fluids. 2005;39(6):p. 1096–1100.

[26] Lorenzoni V. Aeroacoustic Investigation of Rod-Airfoil Noise based on Time-Resolved PIV. Delft University of Technology. the Netherlands; 2008.

[27] Troolin D, Longmire E, Lai W. Time resolved PIV analysis of flow over a NACA 0015 airfoil with Gurney flap. Experiments in Fluids. 2006;41(2):p. 241–254.

[28] Kato C, Iida A, Takano Y, Fujita H, Ikegawa M. Numerical prediction of aerodynamic noise radiated from low mach number turbulent wake. AIAA paper. 1993;p. p. 93–145.

[29] Oreslli R, Meneghini JR, Saltara F. Two and three-dimensional simulation of sound generated by flow around a circular cylinder. In: 15th AIAA/CEAS Aeroacoustics Conference, AIAA. vol. 3270; 2009. .

[30] Pröbsting S, Scarano F, Bernardini M, Pirozzoli S. On the estimation of wall pressure coherence using time-resolved tomographic PIV. Experiments in fluids. 2013;54(7):p. 1–15.